POLITECNICO DI TORINO
Repository ISTITUZIONALE

Physical Characterization of the Effects of Downstream Porosity on Leading-Edge Noise Generation and Reduction

Original
Physical Characterization of the Effects of Downstream Porosity on Leading-Edge Noise Generation and Reduction / Bevilacqua, U., Piccolo, A., Zamponi, R., Palleja-Cabre, S., Avallone, F.. - (2026). (32nd AIAA/CEAS Aeroacoustics Conference (2026) Brussels (BEL) 26-29 May 2026) [10.2514/6.2026-3488].

Availability:
This version is available at: 11583/3011190 since: 2026-06-15T09:44:41Z

Publisher:
American Institute of Aeronautics and Astronautics, Inc.

Published
DOI:10.2514/6.2026-3488

Terms of use:

This article is made available under terms and conditions as specified in the corresponding bibliographic description in the repository

Publisher copyright

(Article begins on next page)

16 September 2026

Physical Characterization of the Effects of Downstream Porosity on Leading-Edge Noise Generation and Reduction

Umberto Bevilacqua*
Politecnico di Torino, Torino, 10129, Italy

Andrea Piccolo†
Delft University of Technology, Delft, 2629HS, Netherlands

Riccardo Zamponi‡
Delft University of Technology, Delft, 2629HS, Netherlands
von Karman Institute for Fluid Dynamics, Sint-Genesius-Rode, B-1640, Belgium

Sergi Palleja-Cabre§
Institute of Sound and Vibration Research, University of Southampton, Southampton, SO17 1BJ, UK

Francesco Avallone¶
Politecnico di Torino, Torino, 10129, Italy

A numerical investigation has been conducted to characterize the reduction of noise generated by the interaction of incoming turbulence with a flat plate featuring a porous region downstream of the leading edge (referred to as downstream porosity). This work builds on previous experimental and analytical studies where promising noise reduction was achieved and several physical mechanisms potentially contributing to it were identified. These include phase inversions of pressure jumps potentially linked to secondary vorticity phenomena, destructive interference between noise sources, and the alteration of coherent structures within the boundary layer. The present work aims to investigate these mechanisms in detail, corroborating and extending novel experimental findings, to quantify their relative contributions to noise reduction and correlate them with the flow behavior within the perforation holes. The analysis of the unsteady surface pressure over the porous region reveals a marked, periodic phase opposition with respect to the primary noise source at the flat-plate leading edge, persisting across the entire porous section. This behavior indicates that destructive interference underlies the noise-reduction peaks observed experimentally, providing the first evidence for this mechanism. The analysis of the vorticity field, together with the velocity and surface-pressure spectra, supports the presence of a coherent mechanism over the porous region that is associated with this phase opposition. However, its origin and nature remain to be clearly established.

I. Introduction

The reduction of noise emissions constitutes a primary research goal in the aviation sector, driving extensive efforts to develop mitigation strategies and improve prediction capabilities. Turbulence–interaction noise (also referred to as leading-edge or inflow-turbulence noise), caused by the interaction between an aerodynamic surface and incoming turbulent structures, is of particular importance due to its relevance across a wide range of applications, including wind turbines, ventilation fans, unmanned aerial vehicle (UAV) rotors, and aeroengine outlet guide vanes (OGVs) [1]. As a result, it represents one of the most extensively studied sources of flow-induced noise. Research on mitigation strategies for this mechanism has primarily focused on two approaches: leading-edge serrations and porous media [2, 3]. While leading-edge serrations have demonstrated only limited acoustic benefits, often accompanied by significant aerodynamic penalties [4], the potential advantages of porous treatments remain under active investigation.

*MSc, Department of Mechanical and Aerospace Engineering, s314120@studenti.polito.it
†Post-Doctoral Researcher, Flow Physics and Technology Department, a.piccolo@tudelft.nl.
‡Assistant Professor, Flow Physics and Technology Department, r.zamponi@tudelft.nl, AIAA Member.
§Senior Research Fellow, Acoustics Group, Institute of Sound and Vibration Research, s.palleja-cabre@soton.ac.uk
¶Full Professor, Department of Mechanical and Aerospace Engineering, francesco.avallone@polito.it, AIAA Member.

The study of Geyer et al. [5] was among the first to investigate this technology for leading-edge noise reduction. In that work, a fully porous airfoil interacting with a turbulent flow demonstrated significant noise reduction with increasing flow resistivity. However, this benefit was accompanied by a degradation in aerodynamic performance. A different configuration with an airfoil with perforations at the leading edge was investigated later by Geyer et al. [6]. Noise reduction of 8 dB in the mid-frequency range was obtained; however, a detrimental effect on the aerodynamics was also observed, at least at high angles of attack. The experimental study confirmed that noise reduction arises from both turbulent kinetic energy dissipation and the attenuation of surface pressure fluctuations associated with the displacement of incident turbulent structures.

Zamponi et al. [7] investigated the physical mechanisms underlying noise reduction in porous configurations, measuring the acoustic emission induced by the impingement of vortex shedding generated by an upstream cylinder on a NACA airfoil with a porous leading edge. The reduction in turbulence-interaction noise at low frequencies (accompanied by an increase at high frequencies due to surface roughness [8]) was associated with decreased vertical velocity fluctuations, leading to a reduction in surface pressure fluctuations [9]. In addition, a less efficient sound conversion was attributed to a less pronounced distortion of the fluid near the airfoil, caused by permeability at the leading edge [10].

Chaitanya et al. [11] compared the noise-generation mechanisms of fully and partially porous flat plates, showing that additional mechanisms become significant for thin-profile configurations such as OGVs. Two types of acoustic sources were identified. The first is the compact pressure jumps at the leading and trailing edges of the porous region of length l, present only for the partially porous plate. The second is a pressure jump distributed over the porous region, present in both configurations. Noise reduction was observed and two different mechanisms were identified as contributing to it. The first, present in both configurations, is the "cutoff" (i.e. the non-propagation of evanescent modes), which produces reduction peaks at integer Strouhal numbers $fl/U_\mathrm{c} = n$, where U_c is the convection velocity evaluated as 70% of the free-stream velocity U_∞. This mechanism arises from subcritical acoustic waves whose convection velocity is lower than the speed of sound. The second, specific to the partially porous configuration, is the destructive interference between compact sources, which causes reduction peaks at $St = n - 1/2$, with St evaluated as $St = fl/U_\infty$.

Since leading-edge porosity often imposes an aerodynamic performance penalty [12], configurations incorporating a porous treatment extending from l_0 to l_d downstream of the leading edge have recently attracted significant research attention. Palleja-Cabre et al. [13] investigated this approach for a flat plate at zero incidence, aiming to identify noise-reduction mechanisms and assess whether such configurations could mitigate aerodynamic losses. Their study reported notable noise-reduction performance, which was attributed to two mechanisms: a phase-inversion effect between the compact source at the leading edge and secondary sources across the porous zone, and a reduction in the spatial extent of the scattering surface upstream of the porous region. Acoustic measurements confirmed reduction peaks at $fl_\mathrm{d}/U_\mathrm{c} = n$ and revealed a strong similarity between the flat plate with downstream porosity and the *tandem* configuration, in which the porous region is replaced by an empty gap. In this context, the phase inversion was attributed to secondary vorticity rotating opposite to that of the primary vortex incident on the leading edge. However, this interpretation rests on two assumptions: equal intensity of the compact sources and frozen advection of the secondary vorticity. The latter phenomenon may be associated with nonlinear effects contributing to the flow dynamics and noise generation over the porous region [14, 15], or with the emergence of coherent structures [16].

This work aims to provide a physical description of the mechanisms governing leading-edge noise generation in downstream porosity configurations. For this purpose, a numerical investigation has been carried out using the lattice-Boltzmann method (LBM) solver PowerFLOW. The simulations, which do not employ a porosity model, aim to complement and extend the experimental study conducted in the anechoic wind tunnel at Delft University of Technology, on which the numerical setup is based. Together, the experimental and numerical approaches seek to validate and further develop the physical explanation advanced by Palleja-Cabre et al. [13] for the noise-reduction mechanisms observed in such configurations.

The paper is organized as follows. Section II introduces the flow solver and numerical setup. Section III presents the results, and Section IV summarizes the conclusions.

II. Methodology

A. Flow Solver

The commercial software Simulia PowerFLOW 6-2021 has been used to compute the flow field. The software is based on LBM and employs the "immersed boundary method" technique, which offers significant advantages with

respect to traditional body-fitted methods [17, 18]. The LBM model [19] describes a fluid at the mesoscale level through a process of advection and collision between particles that alters the particle distribution function. This spatial and temporal alteration is described by Boltzmann's equation in the form:

$$(\partial_t + c_\alpha \partial_\alpha) f = \Omega[f]. \tag{1}$$

f represents the distribution of n particles and takes into account the correlations between them, c_α is the particle speed, and Ω is the collision operator. Eq. 1, unlike the equations used in its proof, is time-asymmetric, which means that it cannot be reversed in time [19]. There is thus a single temporal direction and thus a single time scale τ during which equilibrium conditions tend to be reached [20]. This means that the Boltzmann equation can be rearranged such that the collision operator (which indicates the forces exchanged between two particles and the levels of probable correlation between multiple particles involved in the collision) $\Omega[f]$ can be expressed as

$$\partial_t f + c_\alpha \partial_\alpha f = -\frac{1}{\tau}(f - \bar{f}). \tag{2}$$

In other words, during the collision, there is a relaxation of the distribution functions (f, hence tends to $\bar{f}$) which occurs in a time τ. This is the Bhatnagar, Gross, and Krook (BGK) equation. The discrete formulation of the BGK equation is as follows:

$$f_i\left(\mathbf{r} + \mathbf{c}_i, t + 1\right) - f_i(\mathbf{r}, t) = \Omega_i(\mathbf{r}, t), \tag{3}$$

which describes a process of advection (zero collision operator) and collision (non-zero collision operator) of particles moving on a 3D lattice in 19 precise directions (D3Q19). The transition from Eq. 3, which analyzes the mesoscale, to the NS equation (macroscale) is made using the 3$^{\text{rd}}$ order Chapman-Enskog expansion. This consists of expanding both the time derivatives and the probability functions f using the Knudsen number as the expansion coefficient [19]. Regarding the collision operator, the most commonly used formulation is the one that approximates the continuous BGK formulation, as in Eq. 2, with the expansion of f^{eq} to the second order [21]:

$$f_i^{\text{eq}} = \rho\omega_i \left[1 + \frac{\boldsymbol{V}_i \boldsymbol{u}}{\mathrm{a_s^2}} + \frac{(\boldsymbol{V}_i \boldsymbol{u})^2}{2\mathrm{a_s^4}} - \frac{|\boldsymbol{u}|^2}{2\mathrm{a_s^2}}\right], \tag{4}$$

where a_s is non-dimensional speed of sound in lattice unit.

PowerFLOW uses a LBM-VLES (Very Large Eddy Simulation) turbulence model for all flow types to resolve structures below the grid filter [22, 23], employing the two equations of the Re-Normalisation Group (RNG) $k - \epsilon$ model. The adopted model is a variant of the classic $k - \epsilon$ formulation [24], which improves its accuracy in complex flows through modifications such as the addition of terms in the epsilon transport equation and reduced standardization in the calculation of the Prandtl number. In lattice methods, such as the one used in PowerFLOW, the effects of sub-grid structures are taken into account through an effective relaxation time [22], which involves adding a term linked to turbulent modeling:

$$\tau_{\text{effective}} = \tau_0 + \tau_{\text{turb}}\,, \quad \tau_{\text{turb}} = C_\mu \frac{k^2}{\varepsilon} \frac{1}{T\sqrt{1 + \tilde{\eta}^2}}, \quad \widetilde{\eta} = \psi\left(\eta_s, \eta_\Omega, \eta_h \ldots .\right), \tag{5}$$

where $C_\mu = 0.08$ and τ_0 is the viscous relaxation time, $\bar{\eta}$, indicative of the time scale of the flow and indicating the uniformity of the turbulence pattern at all flows. Regarding the Reynolds stresses, in LBM solvers, these are not added explicitly but arise automatically through the concept of relaxation towards a state of equilibrium (f_{eq}) according to the gas kinetic theory [25].

PowerFLOW divides the fluid domain into refinement zones composed of three-dimensional blocks, or *voxels*, whose size changes between successive voxel refinement (VR) regions by a factor of two. The intersection of solid bodies with the voxels creates surface elements called *surfels*, whose interaction with the fluid particles occurs according to non-slip (bounce-back process) or slip (specular reflection) boundary conditions [23].

Far-field acoustic pressure is obtained using the Ffowcs Williams and Hawkings (FWH) acoustic analogy, implemented in the Farassat 1A formulation [26].

Table 1 Key Features of Flat Plate

Parts	Chord	Span	Holes number	Holes diameter	Thickness
Flat Plate	c_0 = 190 mm	S = 480 mm	9 rows	Φ_i = 3 mm	t = 3 mm

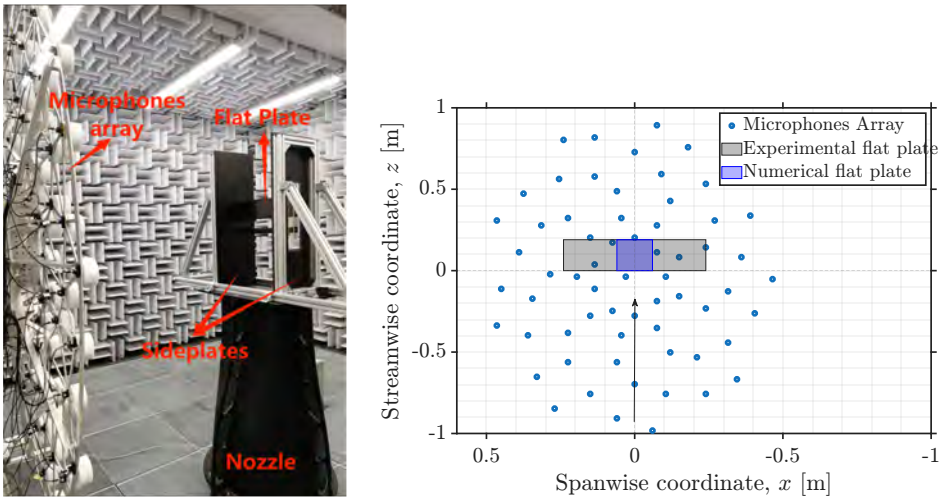

(a) (b)

Fig. 1 (a) Experimental Setup in TU Delft;(b) Microphones position in the beamforming array

B. Simulation setup

1. TU Delft experimental setup

The numerical setup developed for this study replicates the experimental configuration at TU Delft, shown in Fig. 1(a). This campaign was aimed at continuing the investigation previously conducted by Palleja-Cabre et al. [13]. The experimental setup consists of an open-jet wind tunnel placed inside an anechoic chamber (referred to as “A-Tunnel"), whose walls and ceiling are covered with wedges made of absorbent material, as described in detail in Merino-Martínez et al. [27]. The nozzle of the open-jet wind tunnel is 1 m long and features a circular inlet section of approximately 0.28 m^2 and a rectangular outlet section of 0.1 m^2. The flat plate is located 0.3 m downstream of the nozzle outlet, where a rectangular turbulence-generating grid is placed. The turbulence grid is made of square rods with a cross-section l =2 $\times$ 10^{-3} m thick, with a spacing W of 0.010 m, leading to a porosity β of 0.69 and a mesh length M of 0.012 m. The flat plate, made using a 3D printer, has a span of 0.48 m, of which approximately 0.01 m on each side are dedicated to the mounting of the support side plates. The chord is equal to 0.19 m and both the leading edge and trailing edge are chamfered. At a distance of 0.027 m from the leading edge, there is the axis of the hole belonging to the first row of 9. Each hole is imagined at the center of 0.005 m squares, adjacent to each other in both the spanwise and streamwise directions (see Fig. 2). The distance between the centers of the first and last holes is 0.040 m; each hole has a diameter of 0.003 m and extends across the entire 0.003 m thickness of the flat plate.

Acoustic measurements have been obtained by means of the beamforming array shown in Fig. 1(b). This array features 7 spiral arms of 9 microphones each. The array is parallel to the flat plate at a distance of 1.17 m, centered on the midspan of the flat-plate leading edge. More information about the beamforming array is available in Merino-Martínez et al. [27].

Aerodynamic measurements have been carried out by means of time-resolved PIV with a sampling frequency of 16 480 Hz and a spatial resolution of 0.2576 $\times$ 10^{-3} m. The field of view (FOV) extends from approximately 3 $\times$ 10^{-3} m upstream of the LE to beyond the entire porous zone.

2. Numerical setup

The numerical domain consists of a thin parallelepiped with dimensions, expressed in terms of the chord length c, of $37c$ in the streamwise direction and $24c$ in the vertical direction. A width of 0.12 m was chosen, which is smaller than the span of the flat plate to achieve higher spatial resolution near the porous region while keeping the overall computational cost low. Periodic boundary conditions were applied on the lateral faces of the domain.

The domain width was selected to preserve the correct periodicity of both the turbulence-grid pattern and the perforated region of the flat plate, while also avoiding any constraint on the development of homogeneous and isotropic turbulence. In this regard, Blackmore et al. [28] has defined a pattern of at least $3\,\mathrm{M} \times 3\,\mathrm{M}$, with M being the turbulence grid mesh length. The A-Tunnel nozzle has been prolonged upstream to move the flat plate further away from the inlet wall and avoid the reflection of acoustic waves. The reference frame is centered at the midspan of the leading edge, with the streamwise, vertical (upwash), and spanwise directions denoted by z, y, and x, respectively. The corresponding velocity components are indicated as w, v, and u.

The refinement regions (see Fig. 2) have been arranged to maintain a constant voxel size from the turbulence grid to the flat plate to avoid numerical effects in the convection of the turbulent structures. An additional refinement region (indicated as "High resolution" in Fig. 2) has been added around the flat plate, both to achieve a better resolution of the boundary layer controlled by the y^+ parameter and to resolve turbulent structures smaller than 8% of the hole diameter [29]. It should be noted that y^+ has not been imposed but is controlled as an output parameter.

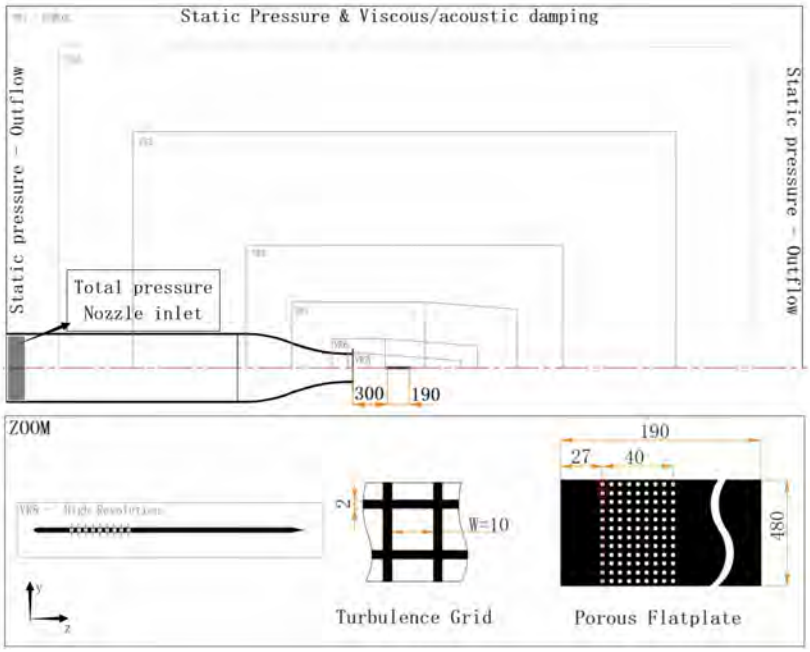

Fig. 2 Refinement regions and boundary conditions in the simulation domain.

The voxel size in the refinement zone that extends from the turbulence grid to the flat plate was determined using the studies of Blackmore et al. [28], which show that almost 32 voxels per mesh length M (turbulence grid parameter) are required to correctly develop turbulence downstream of the grid. At each refinement level, the convergence of the LES simulation will be checked to ensure that, by increasing the discretization, the resolved turbulent kinetic energy tends to at least 80% of the total one [29, 30].

The free-stream velocity was set at $20\,\mathrm{m\,s^{-1}}$, and the total pressure, set as a boundary condition at the inlet, was evaluated taking into account the pressure drop induced by grid turbulence. This has been estimated using the empirical expressions of Roach [31], where the Δp across the rectangular grid, non-dimensionalized with respect to the upstream dynamic pressure q, is expressed as a function of the grid porosity β_{grid} and the coefficients A and B, which are a

Table 2 Comparison of the simulations characteristics.

Refinement level	Nº voxel	CPU time [h]	Voxels/hole	Smallest voxel [m]
Medium	$\sim 0.2 \times 10^9$	1.37×10^4	12.8	2.34×10^{-4}
Fine	$\sim 1.5 \times 10^9$	2.57×10^4	25.5	1.17×10^{-4}

function of the Reynolds number, Mach number, and grid geometry:

$$\frac{\Delta p}{q_\infty} = A\left(\frac{1}{\beta_{\text{grid}}^2} - 1\right)^B .$$

The static pressure was set to 101 325 Pa both inside the fluid volume and on the four side surfaces delimiting the simulation volume. Friction inside the separation cylinder and nozzle was neglected, while these effects are present on the turbulence grid and flat plate. The simulation volume has a high-viscosity fluid zone in the upper and lower parts (indicated in Fig. 2 as "Viscous/acoustic damping"), which is useful for damping acoustic waves and thus limiting the reflection effect on the domain boundaries. The distance of this damping zone from the flat plate was chosen to be sufficiently large to prevent this viscosity from altering the flow through and out of the nozzle.

The simulation time was determined in terms of flow passes (FP), defined as the time it takes for a particle to travel a distance equal to the chord at the free-stream velocity. The convergence of the lift coefficient was chosen as the control variable to define the simulation time. With reference to the highest resolution level, the corresponding simulation, utilizing the seeding technique, included a transient phase of 15 FPs, after which data were saved for 47 FPs, resulting in a total simulation duration of 62 FPs, equivalent to 0.589 s. The sampling frequency chosen for sampling the data in the flow field and on the flat-plate surface is approximately 201.3 kHz.

Two simulations with increasing levels of mesh refinement were performed. Their characteristics are summarized in Table 2.

C. Validation of the numerical simulations

The validation of the numerical simulation is performed by comparing aerodynamic and acoustic data with the experimental measurements of the campaign conducted at TU Delft.

1. Aerodynamic validation

The comparison is conducted in terms of the integral length scale, turbulence intensity, and streamwise velocity spectrum at $z/c = -0.0135$ and $y/c = 0.0863$. The measurement point was placed as far as possible from the flat plate to avoid distortions induced by both numerical factors (boundary-layer modeling, body penetration into the voxels) and experimental limitations (PIV resolution).

The integral length scale of the streamwise-velocity component in the same direction L_{ww}^z has been evaluated by means of the equation 6:

$$L_{ww}^z(\boldsymbol{z}, l) = \int_0^\infty R_{ww}^z(\boldsymbol{m})\mathrm{d}l = \int_0^\infty \frac{\overline{w\,(\boldsymbol{z} + \boldsymbol{l}\boldsymbol{e}_m)\, w(\boldsymbol{z})}}{w(\boldsymbol{z})w(\boldsymbol{z})}\mathrm{d}l, \tag{6}$$

where $R_{ww}^z(\boldsymbol{m})$ is the correlation coefficient calculated considering a reference location z, e_m is the unitary vector in the m-th direction, and $\mathbf{le}_m$ is the separation length from the reference location. The average in the expression formally represents an ensemble average. Given the impracticality of performing such an operation, the ergodicity theorem is invoked so that it can be treated as a temporal or spatial average [32], provided that the flow is, respectively, statistically stationary or homogeneous in the direction of the convolution. In the present case, the well-known statistical homogeneity in the streamwise direction leads to the choice of a spatial average taken along the line at a height of $y/c = 0.0863$, extending from $z/c = -0.0135$ to $z/c = 0.284$.

The turbulent intensity associated with the streamwise fluctuation is indicated as $\mathrm{T}_w = \sqrt{\overline{w'^2}}/\overline{W}_\infty$. This quantity, together with L_{ww}^z, is used as input to the analytical von Kármán model for the streamwise velocity spectrum, reported

Table 3 Comparison of flow parameters obtained from experimental and numerical analyses.

Activity	$\bar{W}_\infty$ (m/s)	L_{ww} (m)	T_w (%)
Experimental PIV	19.18	0.0057	3.3
Present (LBM) *(Medium)*	19.10	0.0062	3.9
Present (LBM) *(Fine)*	19.80	0.0063	3.0

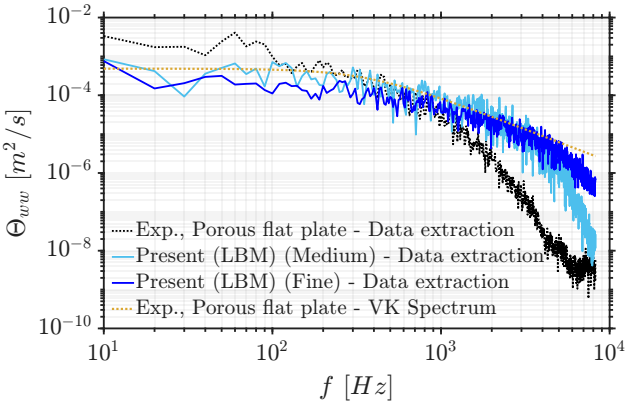

Fig. 3 Comparison between the power spectral densities of the streamwise-velocity component obtained numerically and experimentally.

hereafter:

$$\Theta_{ww}\left(k_z\right) = \frac{1}{\sqrt{\pi}} \frac{\Gamma(5/6)}{\Gamma(1/3)} \frac{\overline{w^2}}{k_\mathrm{e}} \frac{1}{\left[1 + (k_z/k_\mathrm{e})^2\right]^{5/6}}. \tag{7}$$

Γ is the Gamma function, k_z is the wavenumber in the streamwise direction, and k_e is defined as the wavenumber scale of the largest eddies according to the expression:

$$k_\mathrm{e} = \frac{\sqrt{\pi}}{\mathrm{L}^z_{ww}} \frac{\Gamma(5/6)}{\Gamma(1/3)}. \tag{8}$$

The comparison between the time-averaged free-stream velocity, integral length scale, and turbulence intensity obtained numerically and experimentally is reported in Tab. 3, showing good agreement. Figure 3 presents the one-dimensional wavenumber spectrum of the streamwise velocity fluctuations computed numerically, experimentally and analytically using the von Kármán model at the point previously described. The similar trends observed in the spectra obtained from the numerical simulations indicate good grid convergence, consistent with the results reported in Tab. 3. The slight discrepancies at low and high frequencies can be attributed to the shorter simulation time and the narrower grid filter associated with the fine resolution, respectively. A comparison between the spectrum obtained from PIV processing and that derived numerically reveals an overestimation at low frequencies and an underestimation at high frequencies. This behavior is consistent with the findings of Xu and Chen [33], who attributed it to the filtering effect introduced by PIV windowing. The von Kármán (VK) spectrum (Eq. 7), evaluated using parameters derived from the experimental data, is also included as a reference. Notably, it shows better agreement with the numerical spectrum than with the experimental one.

2. Acoustic validation

Acoustic validation was carried out by comparing the far-field sound pressure levels (SPL) computed via the FWH analogy with experimental measurements at four selected microphone positions within the beamforming array. It should be noted that a correction is required to account for the reduced span of the numerical domain, which is $1/4$ the size of the experimental flat plate. Among the various empirical corrections available in the literature, the method proposed by

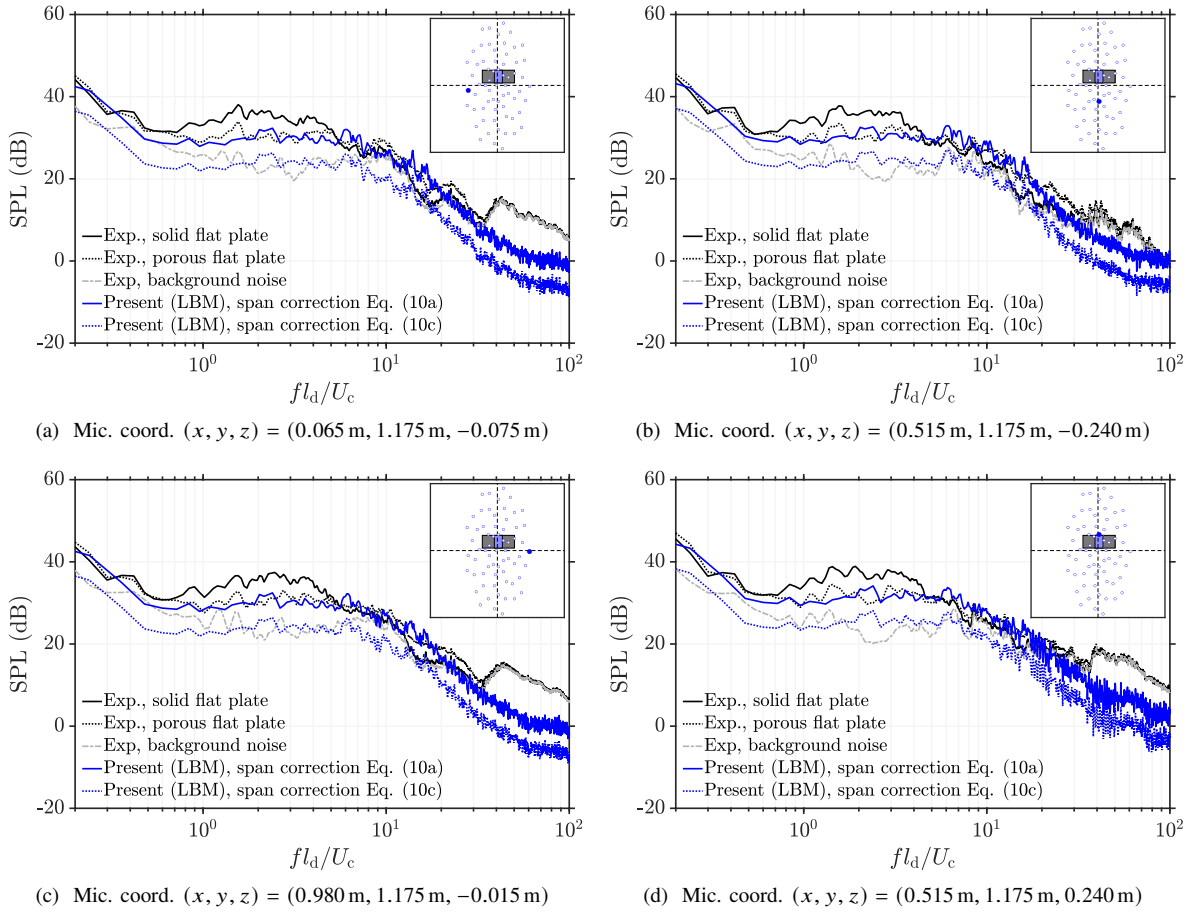

(a) Mic. coord. $(x, y, z) = (0.065\,\text{m}, 1.175\,\text{m}, -0.075\,\text{m})$

(b) Mic. coord. $(x, y, z) = (0.515\,\text{m}, 1.175\,\text{m}, -0.240\,\text{m})$

(c) Mic. coord. $(x, y, z) = (0.980\,\text{m}, 1.175\,\text{m}, -0.015\,\text{m})$

(d) Mic. coord. $(x, y, z) = (0.515\,\text{m}, 1.175\,\text{m}, 0.240\,\text{m})$

Fig. 4 Comparison of the sound pressure levels obtained using the FWH analogy and experimental measurements at four microphone positions in the beamforming array. Measurements for the solid flat plate and background noise are included as references. The numerical spectra are scaled with two different spanwise corrections (see Eq. (10)).

Jiang et al. [30] was selected. This approach specifies that the SPL obtained via the FWH analogy, SPL_{FWH}, must be adjusted by a correction term, SPL_{corr}, as follows:

$$\text{SPL}_{\text{num}} = \text{SPL}_{\text{FWH}} + \text{SPL}_{\text{corr}}. \tag{9}$$

The term SPL_{corr} accounts for the ratio between the spanwise coherence length l_x and the numerical span L_{num}:

$$\text{SPL}_{\text{corr}} = \begin{cases} 10\log_{10}(N) & \left(\frac{l_x}{L_{\text{num}}} \le \frac{1}{\sqrt{\pi}}\right) \quad \text{(10a)} \\ 10\log_{10}(\sqrt{\pi}N) + 10\log_{10}\left(\frac{l_x}{L_{\text{num}}}\right) & \left(\frac{1}{\sqrt{\pi}} < \frac{l_x}{L_{\text{num}}} < \frac{N}{\sqrt{\pi}}\right) \quad \text{(10b)} \\ 20\log_{10}(N) & \left(\frac{l_x}{L_{\text{num}}} \ge \frac{N}{\sqrt{\pi}}\right), \quad \text{(10c)} \end{cases}$$

where $N = L_{\text{exp}}/L_{\text{num}}$ represents the ratio between the experimental span L_{exp} and the numerical span L_{num}. The analysis of the spanwise coherence length at the leading edge, not reported here for brevity, indicates that the first condition holds over most of the frequency range, whereas at low frequencies the third condition appears to be more appropriate.

Fig. 4 reports the corrected numerical SPLs obtained using both the first and third spanwise correction formulations of Eq. (10), compared with the experimental measurements for the porous flat plate. Experimental data for the solid flat

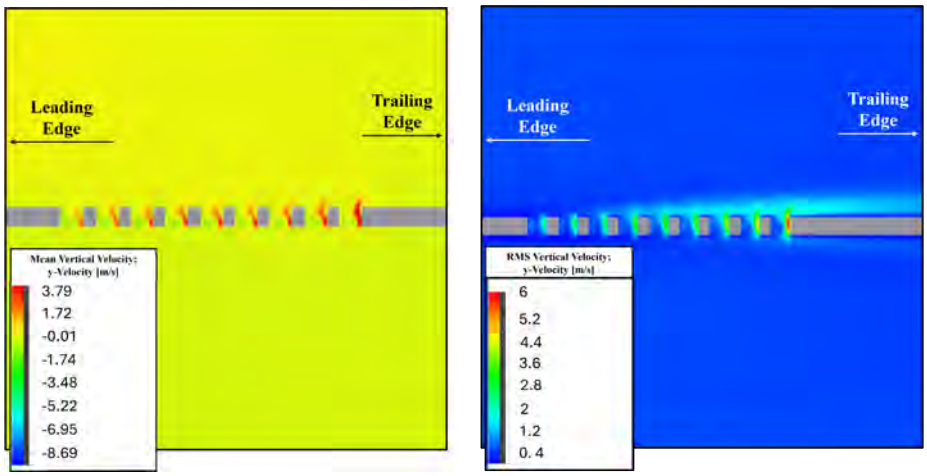

(a) (b)

Fig. 5 Contour plot of the (a) time average and (b) root mean square of the upwash velocity field.

plate and the background noise are also included as references, while the coordinates of the microphones are reported in the subcaption. Although the analysis of the spanwise coherence length would suggest the use of the first spanwise correction, excellent agreement with the experimental results is obtained when the third correction is applied across all microphone positions. It should also be noted that this correction does not account for the presence of the side plates used in the experimental setup to support the flat plate, which are not included in the numerical model.

Regarding the noise reduction obtained with the porous flat plate, the experimental measurements show that, for $St_{l_d} < 10$, the reduction does not exhibit the distinct minima reported by Palleja-Cabre et al. [13] (who, however, evaluated a difference in sound power level (ΔPWL) derived from a directivity arc).

III. Results

A. Analysis of the flow field across the porous region

The flow behavior across the porous region is assessed by visualizing the time-average and the root-mean-square of the upwash velocity component, shown in Fig. 5(a) and Fig. 5(b), respectively. The streamwise velocity component is not reported as it provides limited insight. Interestingly, the visualization reveals an increasing mean and fluctuating flow moving downstream along the porous region. This is consistent with the behavior which can be inferred from the analysis of the streamwise vorticity field. Instantaneous snapshots, shown in Fig. 6, reveal indeed coherent structures that originate at the leading edge of the porous region and amplify downstream. Notably, there is a visible increase in vorticity entrainment from the lower to the upper side of the flat plate.

The frequency spectra of the upwash-velocity component within the pores provide further insight into the evolution of turbulent scales along the porous region. Fig. 7(a) presents a comparison between the velocity spectra sampled at the pore centers (aligned with the upper plate surface) and those obtained upstream of the flat-plate leading edge. The spectra are shown in terms of Strouhal number calculated with respect to the distance between the flat-plate leading edge and the end of the porous region, indicated with l_d, and the convective velocity U_c, obtained as $0.7 \cdot U_\infty$ (and hence equal to $14\,\mathrm{m\,s^{-1}}$). An alternative representation is shown in Fig. 7(b), which presents the spectra as a function of the Strouhal number calculated using the local distance of each pore from the leading edge. The graph illustrates that the upwash motion within the first pore is not weak across the entire spectrum, as might be inferred from Fig. 5(a) and Fig. 5(b); instead, it exhibits a significant drop only within the range $1 \leq St_{z_n} \leq 3$. At $St_{z_n} = 4$, the spectrum sampled at the first row of pores features a prominent peak, which can be traced back to a coherent mechanism triggered at the upstream edge of the porous region. As the flow progresses downstream toward the subsequent pores, the peak is no longer observed, and energy recovers across all frequencies.

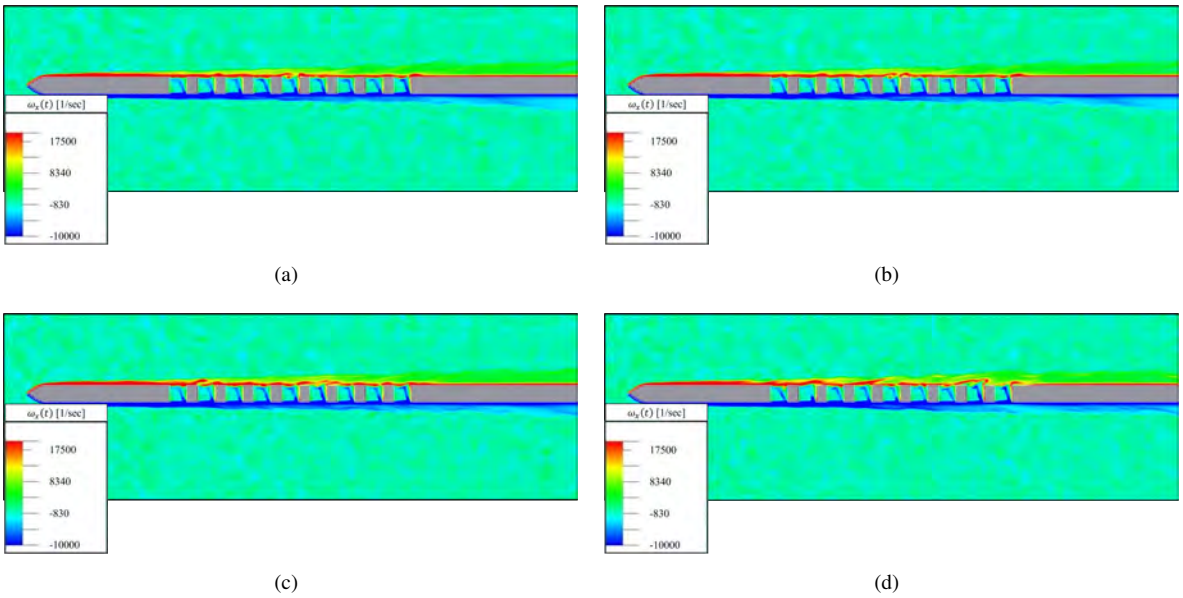

Fig. 6 Contour plots of instantaneous spanwise vorticity fields ω_x at (a) $t_0 = 0.189259$ ms, (b) $\Delta t = 0.103$ ms, (c) $\Delta t = 0.568$ ms, (d) $\Delta t = 2.06$ ms. The snapshots are selected to represent the flow mechanisms developing across the porous region.

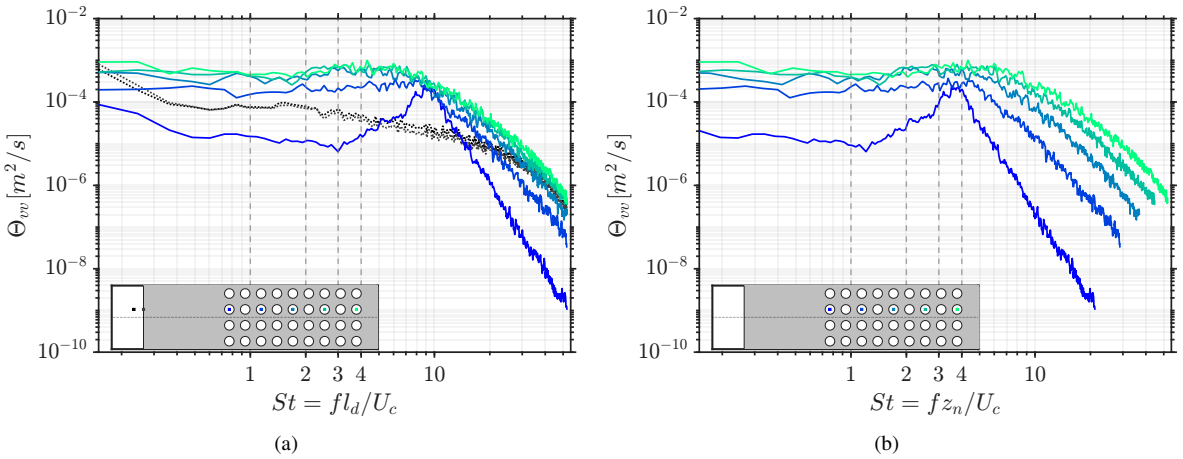

Fig. 7 Turbulence-frequency spectra of the upwash velocity evaluated flush with the flat-plate upper side at each pore center. The Strouhal number is defined using: (a) the distance between the leading edge and the end of the porous region l_d and (b) the distance z between the leading edge and the n-th pore as the characteristic length. The spectra have been spatially averaged in the spanwise direction.

B. Analysis of the noise-generation mechanisms

The connection between the observed flow behavior and noise-generation mechanisms can be inferred by investigating the surface-pressure distribution on the porous region, and considering its coherence and phase with respect to the primary scattering at the leading edge.

The contour plot of the root-mean-square of the surface-pressure fluctuations, reported in Fig. 8 for both sides of the flat plate, shows that the flow mechanism developing across the porous region causes a gradual increase of the fluctuations in the downstream direction. Notably, the amplitude of the fluctuations at the downstream end of the porous region is nearly comparable to that at the leading edge of the flat plate. Although the scattering from this point

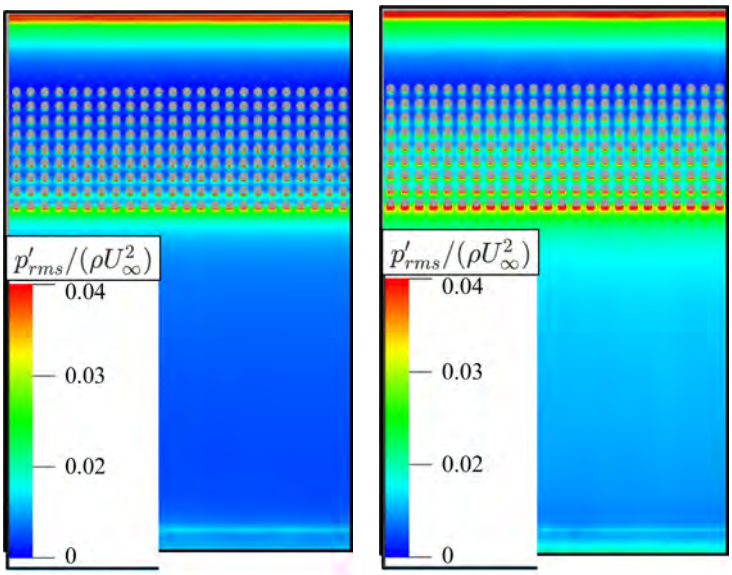

(a) (b)

Fig. 8 Contour plot of the root-mean-square of the surface-pressure fluctuations ($p'_{rms}/(\rho U_\infty^2)$)on the flat plate on the (a) upper side, and (b) lower side.

remains to be characterized, this observation could explain the similar noise reduction observed between the present configuration and the *tandem* one discussed by Palleja-Cabre et al. [13].

Figure 9 presents the frequency spectra of surface-pressure fluctuations on the upper and lower sides of the flat plate, as well as the spectrum of the surface-pressure difference between the two sides. The spectra are evaluated at the downstream side of each pore and compared against the spectrum measured at the flat-plate leading edge, used as a reference. Starting from the spectrum at the first row of holes, a clear collapse with respect to the leading-edge spectrum is observed in the low-frequency range, similar to the upwash velocity spectrum described above (Fig. 7). This is likely due to the restricted flow communication through the porous medium. In contrast, no significant differences are observed at high frequencies. Notably, a mild peak appears at $St_{l_\mathrm{d}} \simeq 10$, which may indicate coherent surface-pressure fluctuations associated with the onset of coherent flow mechanisms at the beginning of the porous region. Moving toward the downstream end of the porous region, a gradual increase in fluctuations is observed across the entire frequency range. In these spectra, a mild peak is also present, but at lower non-dimensional frequencies ($St_{l_\mathrm{d}} \simeq 4$) compared to the spectrum at the first row of holes. The appearance of this lower-frequency peak may indicate either a concurrent coherent mechanism distinct from that associated with the peak at $St_{l_\mathrm{d}} \simeq 10$, or the growth to larger scales of the same coherent mechanism triggered within the porous region.

The surface-pressure spectra can also be represented using an alternative non-dimensional frequency, as done for the velocity-component spectra. Fig. 10 shows the spectra of the surface-pressure difference between the two sides of the flat plate with respect to the non-dimensional frequency scaled with the distance between the leading edge and the streamwise position of each pore. In this representation, although the peaks do not occur exactly at the same frequency, they fall within a narrow range ($St_{z_n} \simeq 2$–4), supporting the hypothesis of a single coherent mechanism triggered in the porous region and developing along it while inducing coherent pressure fluctuations. It is important to note how the peak at $St_{l_d} = 10$ in Fig. 9 and then at $St_{z_n} = 4$ in Fig. 10 is consistent with the peak at the same frequency in Fig. 7(a) and in Fig. 7(b), where the upwash-velocity component is considered. This connection can be traced back to the impingement upon the downstream edge of the vortices shed from the upstream edge of the hole.

The possible contribution of these surface-pressure fluctuations to noise generation can be assessed by examining their coherence and phase with those at the leading edge, where the primary scattering occurs. Fig. 11 presents this comparison for surface-pressure fluctuations on the upper side of the flat plate (Fig. 11(a)), on the lower side (Fig. 11(b)), and for their difference (Fig. 11(c)). The latter is also shown in Fig. 12 using the alternative non-dimensional frequency fz_n/U_c.

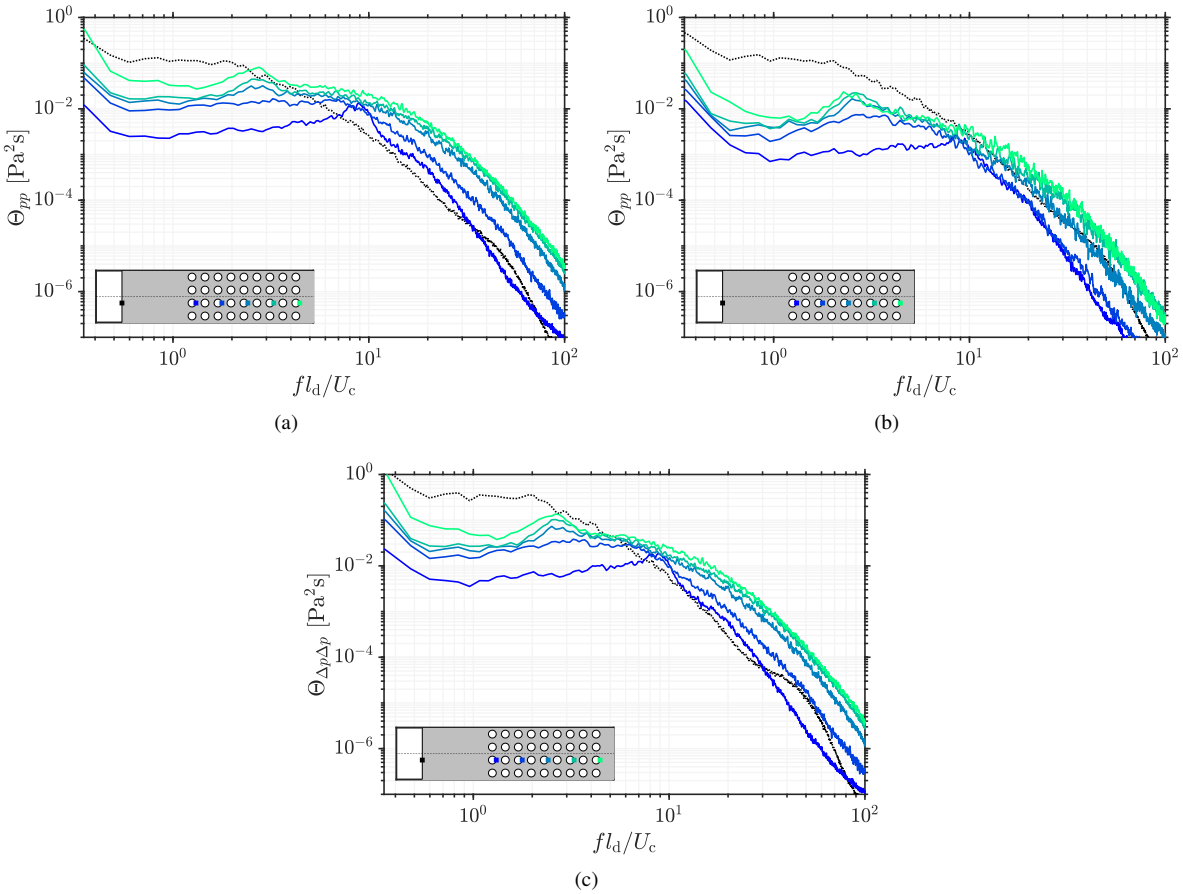

Fig. 9 Surface-pressure spectra at the leading edge compared to the ones at the downstream side of the pores, computed for the upper side ((a)), the lower side ((b)), and their difference ((c)). The Strouhal number is defined using the distance between the leading edge and the end of the porous region l_d. The spectra have been spatially averaged in the spanwise direction.

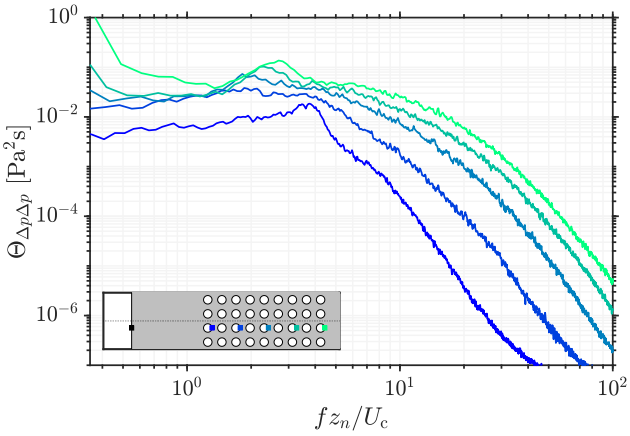

Fig. 10 Surface-pressure-difference spectra evaluated at the downstream side of the pores. The Strouhal number is defined using the distance z between the leading edge and the n-th pore as the characteristic length. The spectra have been spatially averaged in the spanwise direction.

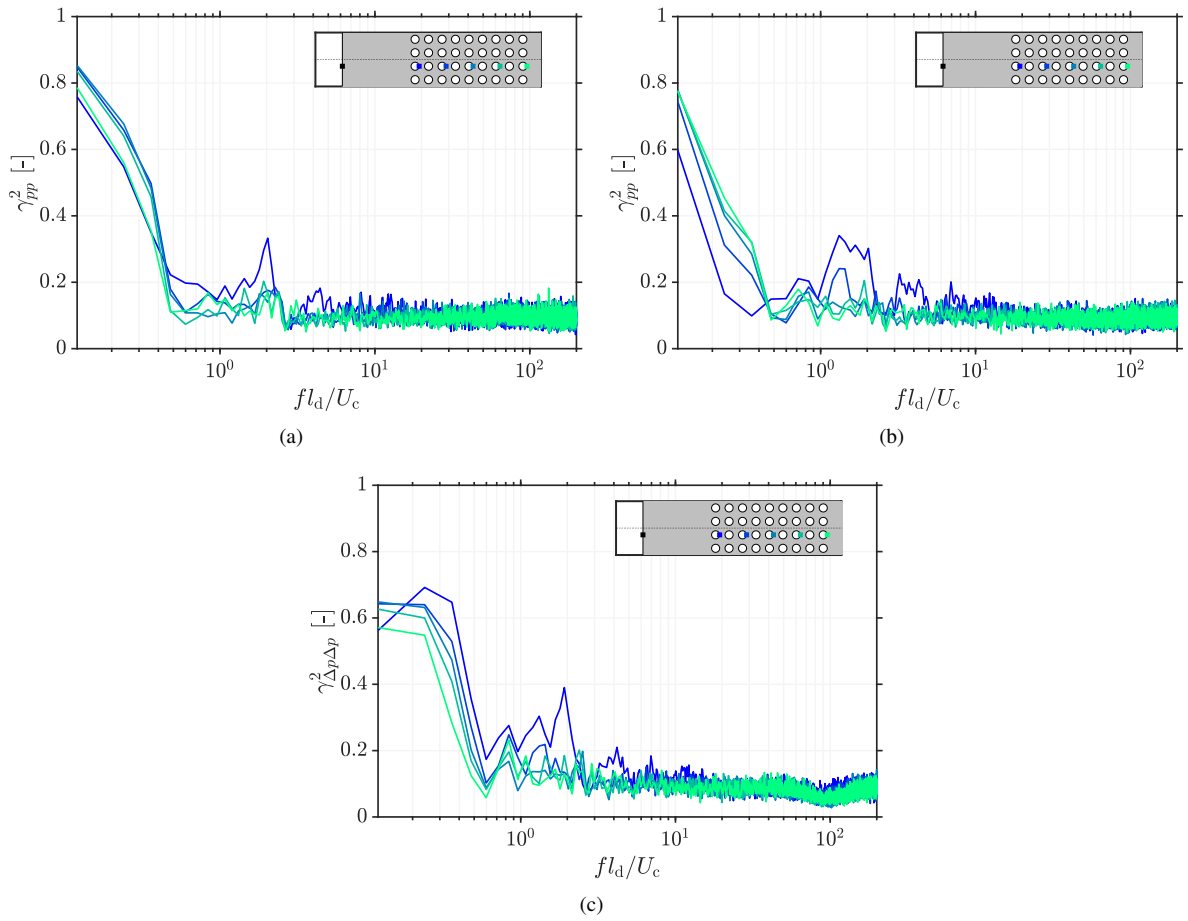

Fig. 11 Magnitude-squared coherence between surface pressure at the leading edge and at the downstream side of the pores, computed for the upper side ((a)), the lower side ((b)), and their difference ((c)). The Strouhal number is defined using the distance between the leading edge and the end of the porous region l_d. The spectra have been spatially averaged in the spanwise direction.

For all sampling configurations, the coherence between fluctuations at the first row of holes and at the leading edge exhibits several pronounced peaks at $St_{l_d} \simeq 2, 4, 8, 10$. These peaks progressively diminish when coherence is evaluated further downstream within the porous region, while coherence at lower frequencies is retained. This behavior is consistent with the evolution of coherent turbulent structures, whereby larger scales preserve coherence as they convect downstream, whereas smaller scales progressively dissipate. Interestingly, when using the alternative non-dimensional frequency, the coherence peaks are found to occur at integer values of St_{z_n}.

Figure 13 shows the phase difference between the surface-pressure fluctuation difference at each pore and the leading edge. The phase is plotted as its cosine to facilitate interpretation and is presented using the alternative non-dimensional frequency directly. The different curves are plotted separately to avoid cluttering the figure, while a grey-scale background trace is retained to aid comparison. Notably, a strong cyclic phase opposition is observed at the first row of holes at integer values of St_{z_n}. This phase opposition, extending beyond $St_{z_n} = 10$, persists when considering more downstream surface-pressure fluctuations and continues to occur at integer values of St_{z_n}. The presence of the pronounced phase inversion between the leading edge of the airfoil and the downstream edge of each hole confirms the hypothesis in Palleja-Cabre et al. [13] that these two sources radiate with a π phase change, and is consistent with the noise-reduction peaks reported in their work.

The PWL of the far-field noise generated by the porous flat plate is shown in Fig. 14. While the absence of results for a solid flat plate prevents a direct assessment of the noise reduction, it is evident that the noise-reduction peaks are less pronounced than those reported in the experimental measurements of Palleja-Cabre et al. [13]. This is actually consistent

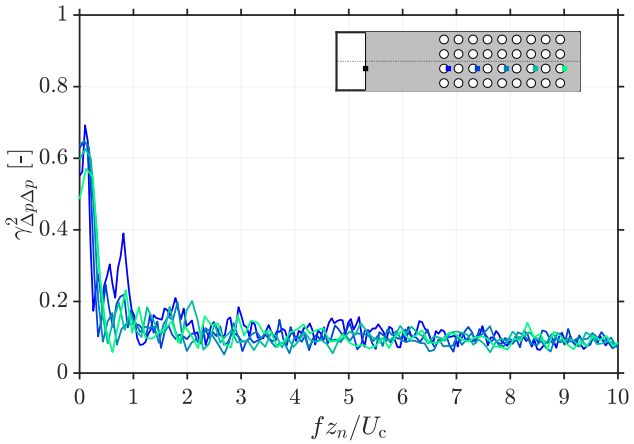

Fig. 12 Magnitude-squared coherence between the surface-pressure difference at the leading edge and at the downstream side of the pores. The Strouhal number is defined using the distance z between the leading edge and the n-th pore as the characteristic length. The spectra have been spatially averaged in the spanwise direction.

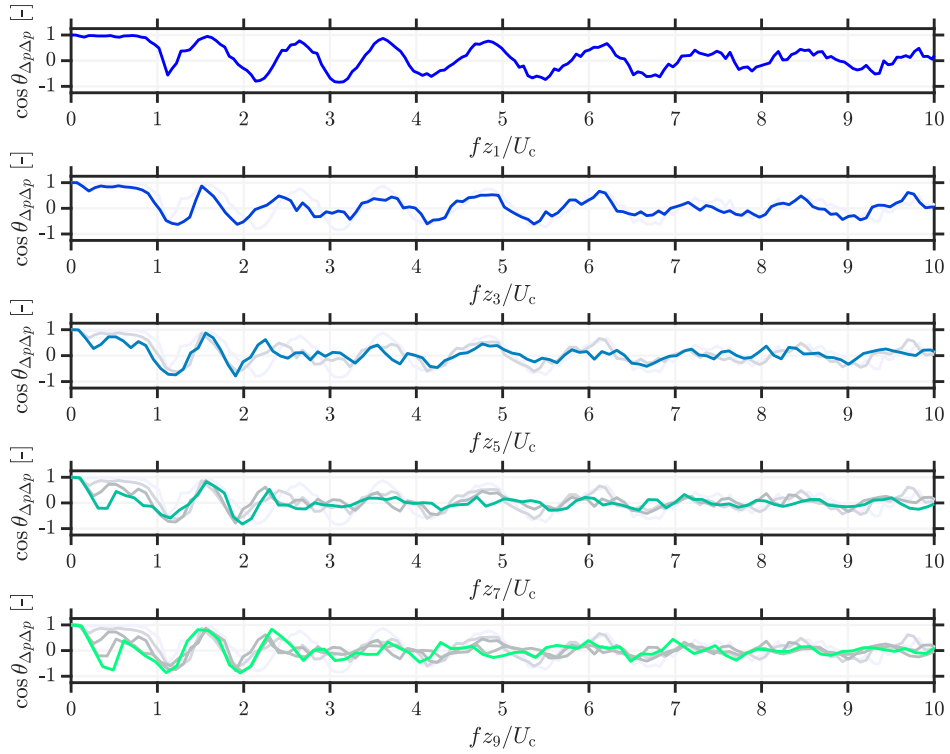

Fig. 13 Phase difference between pressure differences evaluated at the leading edge and at the downstream edge of the pores. The Strouhal number is defined using the distance z between the leading edge and the n-th pore as the characteristic length. The phase spectra have been spatially averaged in the spanwise direction.

with the experimental SPLs reported in Fig. 4. At the same time, weak peaks at $St_{l_d} \simeq 1, 2, 6$ can be identified, which may reflect residual signatures of coherent surface-pressure fluctuations over the porous region. Further investigations are required to clarify the nature of the observed noise reduction and to relate the mechanisms developing over the porous region to the resulting acoustic emissions.

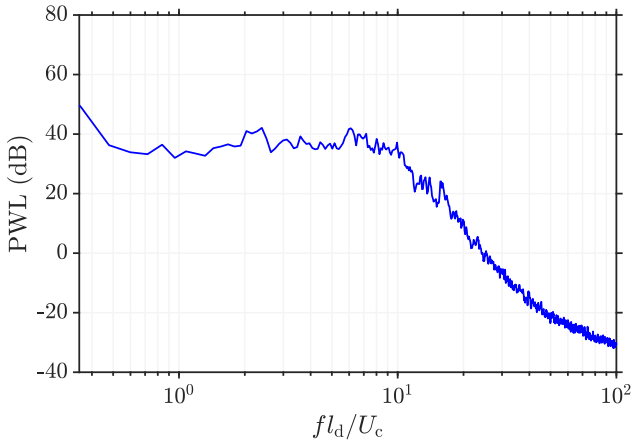

Fig. 14 Sound power level in the far-field for the porous flat plate. The PWL is shown with respect to the Strouhal number calculated with respect to the distance between the leading edge and the end of the porous region l_d and using the convective velocity $U_\mathrm{c} = 0.7 \cdot U_\infty = 14\,\mathrm{m\,s^{-1}}$. The reference power used to calculate the PWL is 1×10^{-12} W.

IV. Conclusions

A numerical investigation has been carried out to physically characterize the noise-reduction mechanisms observed for a flat plate with downstream porosity. The study, performed using the LBM solver PowerFLOW, replicates the experimental campaign conducted in the anechoic wind tunnel at TU Delft and builds upon the previous work of Palleja-Cabre et al. [13].

The results indicate that a coherent mechanism is triggered at the porous region and develops progressively across it. This mechanism induces coherent surface-pressure fluctuations throughout the porous surface, which exhibit both coherence and phase opposition with respect to the unsteady pressure at the flat-plate leading edge, potentially explaining the observed noise reduction. In particular, the strong phase opposition already present at the beginning of the porous region is consistent with the noise reduction reported by Palleja-Cabre et al. [13] for a single row of holes. Moreover, while coherence weakens downstream, the phase opposition persists toward the end of the porous region, suggesting that more complex interactions may govern the noise-reduction mechanisms in configurations with more extended porous regions.

Although this persistent and pronounced phase opposition appears to play a key role in the observed noise reduction, the underlying dynamics and the conditions triggering the mechanism are not fully understood yet. Further investigations are therefore required to better characterize the coherent structures developing over the porous region and, ultimately, to enable their analytical modelling and extension to different geometrical configurations.

Acknowledgements

The authors acknowledge the use of the SNELLIUS supercomputer provided by SURF Cooperative as part of the Dutch national e-infrastructure.

References

[1] Zamponi, R., "Investigation of turbulence-surface interaction noise mechanisms and their reduction using porous materials," Ph.D. thesis, Delft University of Technology, 2021. https://doi.org/10.4233/UUID:D332C7E3-87BE-4ED6-AA71-E629EF77E07A.

[2] Moreau, D. J., and Doolan, C. J., "Noise-reduction mechanism of a flat-plate serrated trailing edge," *AIAA Journal*, Vol. 51, 2013. https://doi.org/10.2514/1.J052436.

[3] Chong, T. P., and Vathylakis, A., "On the aeroacoustic and flow structures developed on a flat plate with a serrated sawtooth trailing edge," *Journal of Sound and Vibration*, Vol. 354, 2015. https://doi.org/10.1016/j.jsv.2015.05.019.

[4] Narayanan, S., Chaitanya, P., Haeri, S., Joseph, P., Kim, J. W., and Polacsek, C., "Airfoil noise reductions through leading edge serrations," *Physics of Fluids*, Vol. 27, 2015. https://doi.org/10.1063/1.4907798.

[5] Geyer, T., Sarradj, E., Giesler, J., and Hobracht, M., "Experimental assessment of the noise generated at the leading edge of porous airfoils using microphone array techniques," *17th AIAA/CEAS Aeroacoustics Conference (32nd AIAA Aeroacoustics Conference)*, American Institute of Aeronautics and Astronautics, ???? https://doi.org/10.2514/6.2011-2713, URL https://arc.aiaa.org/doi/10.2514/6.2011-2713.

[6] Geyer, T. F., Lucius, A., Schrödter, M., Schneider, M., and Sarradj, E., "Reduction of turbulence interaction noise through airfoils with perforated leading edges," *Acta Acustica united with Acustica*, Vol. 105, 2019. https://doi.org/10.3813/AAA.919292.

[7] Zamponi, R., Satcunanathan, S., Moreau, S., Ragni, D., Meinke, M., Schröder, W., and Schram, C., "On the role of turbulence distortion on leading-edge noise reduction by means of porosity," *Journal of Sound and Vibration*, Vol. 485, 2020. https://doi.org/10.1016/j.jsv.2020.115561.

[8] Zamponi, R., Van de Wyer, N., and Schram, C. F., "Experimental Investigation of Airfoil Turbulence-Impingement Noise Reduction Using Porous Treatment," *25th AIAA/CEAS Aeroacoustics Conference*, American Institute of Aeronautics and Astronautics, Delft, The Netherlands, 2019. https://doi.org/10.2514/6.2019-2649.

[9] Zamponi, R., Satcunanathan, S., Moreau, S., Meinke, M., Schröder, W., and Schram, C., "Effect of porosity on Curle's dipolar sources on an aerofoil in turbulent flow," *J. Sound Vib.*, Vol. 542, 2023, p. 117353. https://doi.org/10.1016/j.jsv.2022.117353.

[10] Zamponi, R., Moreau, S., and Schram, C., "Rapid distortion theory of turbulent flow around a porous cylinder," *J. Fluid Mech.*, Vol. 915, 2021, p. A27. https://doi.org/10.1017/jfm.2021.8.

[11] Chaitanya, P., Joseph, P., Chong, T. P., Priddin, M., and Ayton, L., "On the noise reduction mechanisms of porous aerofoil leading edges," *Journal of Sound and Vibration*, Vol. 485, 2020. https://doi.org/10.1016/j.jsv.2020.115574.

[12] Remillieux, M., Crede, E., Camargo, H., Burdisso, R., Devenport, W., Rasnick, M., Seeters, P., and Chou, A., "Calibration and Demonstration of the New Virginia Tech Anechoic Wind Tunnel," 2008. https://doi.org/10.2514/6.2008-2911.

[13] Palleja-Cabre, S., Chaitanya, P., Joseph, P., Kim, J. W., Priddin, M. J., Ayton, L. J., Geyer, T. F., and Chong, T. P., "Downstream porosity for the reduction of turbulence–aerofoil interaction noise," *Journal of Sound and Vibration*, Vol. 541, 2022. https://doi.org/10.1016/j.jsv.2022.117324.

[14] Turner, J. M., and Kim, J. W., "Trailing-edge noise generation from a flat-plate aerofoil interacting with a prescribed vortex," *Journal of Sound and Vibration*, Vol. 489, 2020, p. 115654. https://doi.org/https://doi.org/10.1016/j.jsv.2020.115654, URL https://www.sciencedirect.com/science/article/pii/S0022460X20304843.

[15] Abou-Hussein, H., DeBenedictis, A., Harrison, N., Kim, M., Rodrigues, M. A., Zagadou, F., and Howe, M. S., "Vortex-surface interaction noise: A compendium of worked examples," *Journal of Sound and Vibration*, Vol. 252, 2002. https://doi.org/10.1006/jsvi.2001.3833.

[16] Feng, Z., and Ye, Q., "Turbulent boundary layer over porous media with wall-normal permeability," *Physics of Fluids*, 2023. https://doi.org/10.1063/5.0160773.

[17] R.Verzicco, G. I., M.de.Tullio, "Lecture Series on LES and Related Techniques: Theory and Applications." *Immersed Boundary Techniques for Large Eddy Simulation*, VKI, May 13-17 2024.

[18] Ferziger, J. H., Peric, M., and Leonard, A., "Computational Methods for Fluid Dynamics," *Physics Today*, Vol. 50, 1997. https://doi.org/10.1063/1.881751.

[19] Chin, J., "Mesoscale fluid simulation with the Lattice Boltzmann method," Ph.D. thesis, Queen Mary University of London, 2005. URL http://qmro.qmul.ac.uk/xmlui/handle/123456789/1776.

[20] Chen, H., Chen, S., and Matthaeus, W., "Recovery of the Navier-Stokes Equations Using a Lattice-Gas Boltzmann Method," *Physical Review A*, Vol. 45, 1992. https://doi.org/10.1103/PhysRevA.45.R5339.

[21] Chen, H., Chen, S., and Matthaeus, W. H., "Recovery of the Navier-Stokes equations using a lattice-gas Boltzmann method," *Phys. Rev. A*, Vol. 45, 1992, pp. R5339–R5342. https://doi.org/10.1103/PhysRevA.45.R5339, URL https://link.aps.org/doi/10.1103/PhysRevA.45.R5339.

[22] Chen, H., Zhang, R., Gopalakrishnan, P., Li, Y., Fares, E., and Casalino, D., "Recent Advances of the Lattice Boltzmann Method for Transonic Flow," *Conference Presentation*, 2016.

[23] Piccolo, A., Zamponi, R., Avallone, F., and Ragni, D., "Turbulence distortion and leading-edge noise," *Physics of Fluids*, Vol. 36, No. 12, 2024, p. 125183. https://doi.org/10.1063/5.0244627, URL https://doi.org/10.1063/5.0244627.

[24] University of Washington, "Fluent k– Model Notes," https://courses.washington.edu/mengr544/handouts-10/Fluent-k-epsilon.pdf, n.d. Lecture handout, ME 544: Advanced Fluid Turbulence, Department of Mechanical Engineering, University of Washington.

[25] Casalino, D., Grande, E., Romani, G., Ragni, D., and Avallone, F., "Definition of a benchmark for low Reynolds number propeller aeroacoustics," *Aerospace Science and Technology*, Vol. 113, 2021. https://doi.org/10.1016/j.ast.2021.106707.

[26] Farassat, F., "Derivation of Formulations 1 and 1A of Farassat," Tech. rep., 2007.

[27] Merino-Martínez, R., Carpio, A. R., Pereira, L. T. L., van Herk, S., Avallone, F., Ragni, D., and Kotsonis, M., "Aeroacoustic design and characterization of the 3D-printed, open-jet, anechoic wind tunnel of Delft University of Technology," *Applied Acoustics*, Vol. 170, 2020. https://doi.org/10.1016/j.apacoust.2020.107504.

[28] Blackmore, T., Batten, W. M., and Bahaj, A. S., "Inlet grid-generated turbulence for large-eddy simulations," *International Journal of Computational Fluid Dynamics*, Vol. 27, No. 6-7, 2013, pp. 307–315. https://doi.org/10.1080/10618562.2013.819972, URL https://doi.org/10.1080/10618562.2013.819972.

[29] Guerrero, "Turbulence and CFD models: Theory and applications," Tech. rep., Università di Genova, 2023.

[30] Jiang, C., Moreau, D., de Silva, C., and Doolan, C., "Noise generation mechanisms of a micro-tube porous trailing edge," *Journal of Sound and Vibration*, Vol. 571, 2024. https://doi.org/10.1016/j.jsv.2023.118085.

[31] Roach, P., "The generation of nearly isotropic turbulence by means of grids," *International Journal of Heat and Fluid Flow*, Vol. 8, No. 2, 1987, pp. 82–92. https://doi.org/https://doi.org/10.1016/0142-727X(87)90001-4, URL https://www.sciencedirect.com/science/article/pii/0142727X87900014.

[32] Nieuwstadt (†), F., Boersma, B., and Westerweel, J., *Turbulence: Introduction to Theory and Applications of Turbulent Flows*, Springer, United States, 2016. https://doi.org/10.1007/978-3-319-31599-7.

[33] Xu, D., and Chen, J., "Accurate estimate of turbulent dissipation rate using PIV data," *Experimental Thermal and Fluid Science*, Vol. 44, 2013, pp. 662–672. https://doi.org/https://doi.org/10.1016/j.expthermflusci.2012.09.006, URL https://www.sciencedirect.com/science/article/pii/S0894177712002464.